Snowfall in Northern Finland derives mostly from ice clouds

Claudia Mignani[1], Lukas Zimmermann[1], Rigel Kivi[2], Alexis Berne[3], and Franz Conen[1]

[1]Department of Environmental Sciences, University of Basel, 4056 Basel, Switzerland
[2]Space and Earth Observation Centre, Finnish Meteorological Institute, 99600 Sodankylä, Finland
[3]Environmental Remote Sensing Laboratory, Swiss Federal Institute of Technology in Lausanne, 1015 Lausanne, Switzerland

Correspondence: Claudia Mignani (claudia.mignani@unibas.ch) or Franz Conen (franz.conen@unibas.ch)

Abstract. Cloud properties play a critical role in the Arctic surface energy budget. We present ground-level observations of snowfall coinciding with radiosonde launches in Sodankylä (67.367 °N, 26.629 °E) through a period of eight cold months (October–April) in 2019 and 2020. They comprise 7401 depositing snow particles detected by a snowflake camera and 468 radiosonde profiles. Our results show that precipitating clouds were extending from ground to at least 2.7 km in altitude. Approximately one quarter of them were mixed-phase and the rest were likely fully glaciated. Estimations of the cloud top temperatures indicate that in roughly half of the snowfall events ice might have been initiated through heterogeneous freezing. For such cases, the predicted ice-nucleating particle concentrations active at cloud top temperatures could explain the analysed ice crystal particle concentrations observed near ground. In a warmer climate, the relative proportion of solid to liquid cloud particles will probably decrease, with implications on the Arctic radiation balance.

1 Introduction

Snowfall has a major impact on the hydrological cycle in the Arctic. It is a requirement for snow cover, which affects the freshwater supply (Barnett et al., 2005) and the albedo of the Earth's surface (Hall and Qu, 2006). Therefore, it is important to understand which atmospheric conditions are driving snowfall in that region. A prerequisite for snowfall is the atmospheric formation of ice crystals. Primary ice crystal formation can be initiated either by homogeneous or heterogeneous freezing, that is by cloud droplets freezing spontaneously below a temperature threshold of −38 °C (e.g. Murray et al., 2010) or by ice-nucleating particles (INPs) that promote freezing already at warmer temperatures (e.g. Kanji et al., 2017). Once primary ice crystals have formed, other atmospheric ice-related processes may occur, such as ice crystal growth by vapor deposition, riming, secondary ice formation and aggregation (Fukuta and Takahashi, 1999), followed by deposition and accumulation at the surface, if crystals do not vanish before through sublimation in drier air (Nelson and Baker, 1996). These processes depend on microphysical and dynamical conditions that can lead to fully glaciated clouds (Costa et al., 2017), i.e. ice clouds. Arctic warming probably leads to a change from ice clouds to more liquid clouds, whose radiative properties (Shupe and Intrieri, 2004) further accelerate Arctic warming (Tan and Storelvmo, 2019). Clouds containing ice crystals and generating snowfall can be

studied for example with space-borne remote sensing techniques (e.g. Liu, 2008; Mülmenstädt et al., 2015; Kikuchi et al., 2017;
25 Casella et al., 2017), which may be combined with ground observations of precipitation (Hanna et al., 2008). Another approach
is airborne or ground-based remote sensing (e.g. Delanoë et al., 2013; Kneifel and Moisseev, 2020), sometimes combined with
radiosondes (e.g. Silber et al., 2021) and morphological investigation of ice crystals collected in-cloud (Morrison et al., 2011).
Further, radiosondes have been combined with morphological investigations of ice particles collected at ground level in several
studies (Power et al., 1964; Jiusto and Weickmann, 1973; Seo et al., 2015).

30   Pinpointing the origin of even very low-intensity snowfall requires sensitive snowfall detection at ground-level. The simulta-
neous capture of ice particle habits might enable to disentangle some of the microphysical and dynamical conditions, because
ice particles encode atmospheric conditions and duration of growth they were exposed to. The shape, size, degree of riming,
and eventually aggregation of ice particles encode the temperature and relative humidity with respect to ice and liquid water
at which they grew (Nakaya, 1954). According to the current version of Nakaya's habit diagram (Nakaya, 1954; Magono and
35 Lee, 1966; Bailey and Hallett, 2009), rather large and eventually rimed crystals (including needles, stellar plates, two or three
dimensional dendritic crystals, and graupel) are the result of supersaturation with respect to (liquid) water. Below water satura-
tion compact and unrimed ice particles are to be expected (such as plates, columns, radiating plates, or bullet rosettes), which
grow very slowly (Kobayashi, 1961). Riming occurs if supercooled water droplets of certain sizes are present (Mossop, 1978)
and aggregation of snow particles can be significant at $-17\,°C$ and warmer (Hobbs et al., 1974).

40   In the Arctic, observations of precipitating clouds were predominantly made at coastal or marine sites (e.g. Fridlind et al.,
2012; Delanoë et al., 2013; Mioche et al., 2017; Gierens et al., 2020). Unlike coastal or marine sites, which are associated
with high moisture levels, continental regions, such as northern Eurasia, including Northern Finland, are drier and receive
less snowfall. There, cloud conditions are likely different from those at coastal or marine sites. Here, we used the approach
of combining observations of ice particles at the ground with concurrent radiosonde profiles to identify from what type of
45 clouds, ice or mixed-phase, snowfall predominantly occurs in Northern Finland. Our focus is on identifying general patterns.
Therefore, we analyse observations made throughout a total of eight months distributed over two cold seasons.

2   Methodology

The experimental setup was located at the Arctic Space Centre of the Finnish Meteorological Institute (FMI) in Sodankylä, in
Northern Finland (67.367 °N, 26.629 °E; 179 m a.s.l.; Fig. 1).

2.1   Description of the site

The site is surrounded by a rural landscape consisting of coniferous forest and swamp (Hirsikko et al., 2014). It is situated
just above the Arctic Circle. Due to the Gulf Stream, the climate and vegetation are subarctic, although the stratospheric
meteorology is typically arctic (https://fmiarc.fmi.fi/, last access: 31 January 2022). The site is approximately 500 km from
the Atlantic coast in the precipitation shadow of the mountain range along the north coast of Norway with a highest elevation
55 around 1800 m.

In most Scandinavian countries the west coast regions receive more precipitation during the seven colder months (October–April), as compared to the mainland (Fig. 1). In large parts of Finland, including the location of our site, it does not exceed 300 mm. Within Europe, this is comparable to values in large parts of Northern Sweden, Western Russia, Eastern Europe and Eastern Spain.

2.2 Snowfall measurements and ice particle image processing

A Multi-Angle Snowflake Camera (MASC, Particle Flux Analytics, USA; Garrett et al., 2012) took automatically photographs of precipitating ice particles from 28 February 2019 to 7 April 2020. During that time, the instrument was continuously in operation, excluding the summery months (May–September), when snowfall is very rare at the site (see monthly weather parameters in Fig. A1) and during a short technical interruption between 11 and 25 October 2019. Of note, slight modifications to the original MASC instrument (e.g. new emitter box, exchanging external plugging connectors and internal wiring, adding a box enclosing the isolating transformer and the computer) were performed before installation to make it run smoothly according to our needs. The instrument was installed at two meters above ground on the instrument field of the World Meteorological Organization (WMO) solid precipitation intercomparison experiment (SPICE; Nitu et al., 2018). Whenever an ice particle falls through the horizontal measurement cross-section of the instrument (roughly 10 cm^2), three flashlights and cameras (Unibrain Firewire-800 cameras, image resolution: 5 MP, chip size: 8.8 mm x 6.6 mm, focal length: 12.5 mm), which have a 36-deg angle to each other and an identical focal point, are triggered synchronously. Ice particles are captured against a black background. The images are 2448x2048 pixels, resulting in an optic resolution of $\sim$33 μm per pixel for particles in focus (Praz et al., 2017).

In the following, we only used images taken by the central camera. Generally, the ice particles that trigger the camera are captured in the middle of the resulting MASC images. MASC images on which the object or a part of it was outside the more or less central area of 1748x1430 pixels were rejected from further analysis. This selected area resulted from the original image by cropping 300 pixels from the top, 318 pixels from the bottom, and 350 pixels from both sides. Ice particles were automatically detected using a function provided by the Open Source Computer Vision library to identify the contours of bright (threshold at 20 out of 256 brightness values) continuous objects. We only considered objects with an area of least 500 continuous pixels, which is equivalent to a projected area of 0.54 mm^2, as ice particles suitable for further analysis. Smaller objects could generally not be classified according to criteria useful in the context of this study.

The area, position, maximal height, and maximal width of the projected objects larger than 0.54 mm^2 were retrieved from the image. A rectangle encompassing the ice particle was cut from the image and placed, while maintaining the optical size, in the center of a completely black background of a fixed size, i.e. the size of the largest object observed during the overall course of this study. This processing of images made later visual inspection of the large number of mostly small ice particles more convenient. To ensure fast processing of the data, the files of the MASC images and the pre-defined selection images including extracted features were collected in an SQLite database.

2.2.1 Ice particle classification

Ice particle habits were visually classified. Such with an undefinable habit, such as broken off pieces, were classified as non-specific crystals. Single ice particles with unequivocal shape were divided into nine ice crystal classes (see Fig. 7a, i.e. needles,

90 graupel, spatial dendrites, (planar) dendrites, stellar plates, plates, radiating plates, columns, rosettes). Aggregated ice particles were classified as aggregates composed of specific or non-specific single crystals. If aggregates were composed of a single crystal class, we classified them as such. Only aggregates composed of needles, spatial dendrites, dendrites, stellar plates, radiating plates, or rosettes were observed (see Fig. A7). Each ice particle with an unequivocal shape was classified into rimed or unrimed. An ice particle classified as unrimed (rimed) corresponded to a riming degree of $0-1$ ($2-5$) according to

95 Mosimann et al. (1994). Blurred or dark ice particle images were seen as invalid and classified as blurred or dark, respectively.

2.3 Vertical profiles and data processing

As part of the Global Climate Observing System Reference Upper-Air Network (GRUAN; WMO Integrated Global Observing System station identifier 0-20000-0-02836), vertical profiles of temperature, relative humidity with respect to liquid water, pressure, wind speed and direction were measured at the site with Vaisala RS41 radiosondes (Jensen et al., 2016). Radiosondes

100 were launched daily at 11:30 and 23:30 UTC by an automated sonde system (Vaisala AS41 Autosonde system) (Madonna et al., 2020). The radiosondes were launched on balloons with an ascent velocity of approximately 6 m s^{-1} and data was recorded between ground level and an average of 28 km in altitude. According to the manufacturer, the humidity sensor of the radiosondes has a measurement uncertainty of 4% and a response time of < 0.3 s for $+20\,°C$ (< 10 s for $-40\,°C$), 6 m s^{-1}, and 1000 hPa. For temperature and pressure, the sensor measurement uncertainty above 100 hPa are 0.15 °C (with a response

105 time < 0.5 s) and 0.4 hPa (https://www.vaisala.com/sites/default/files/documents/RS41-SGP-Datasheet-B211444EN.pdf, last access: 31 January 2022).

We used the GRUAN data product, which provides validated data and meta-data. The vertical profiles of relative humidity with respect to ice (RH$_{ice}$) were calculated using the saturation vapor pressure ITS90 formulation by B. Hardy (https://www.decatur.de/javascript/dew/resources/its90formulas.pdf, last access: 31 January 2022) and averaged with a vertical resolution

110 of 100 m.

2.4 Ground-based weather parameters

A ground-based weather station provided weather parameters in 10-min time intervals, including temperature, relative humidity with respect to water, wind measurements (at 22 m above ground), air pressure, snow depth, cloudiness, visibility, cloud base height, present weather, and precipitation determined by different instruments operated by the FMI (https://litdb.fmi.fi/luo0

115 015_data.php, last access: 31 January 2022). The values for wind speed and direction were average values over 10-minute intervals. The values for the other parameters were instantaneous values. In the WMO SPICE field, precipitation was measured optically with a Parsivel[2] (OTT HydroMet, UK), which has a measurement accuracy of $\pm\,20\%$ for solid precipitation between 0.001 mm h^{-1} and 1200 mm h^{-1} (https://www.ott.com/products/meteorological-sensors-26/ott-parsivel2-laser-weather-s

ensor-2392/, last access: 31 January 2022), and by weight with a Pluvio[2] (OTT HydroMet, UK), a weighing gauge that has
120 an absolute accuracy of $\pm$ 0.05 mm when averaged over 60 min (https://www.ott.com/products/accessories-109/ott-pluvi
o2-weighing-rain-gauge-963/, last access: 31 January 2022). As a note, both precipitation instruments obtained a reasonable
agreement after reprocessing Parsivel[2] raw data (Boudala et al., 2014).

During the period of measurements (i.e. from 28 February 2019 to 7 April 2020, excluding May to September), local air
temperature at the site was on average $-5.8\,°C$, with minimum and maximum values of $-34.4\,°C$ and $+16.2\,°C$, respectively.
125 Average relatively humid was 87% and the average wind speed at 22 m above ground (i.e. above tree top) was 2.7 m s^{-1}, with a
mean direction from Southwest–WestSouthwest (235 °). Moreover, the ground was covered with snow with a mean snow depth
of 70 cm and the total precipitation during the eight months was 295 or 376 mm, depending on the measurement method (optical
or by weight, respectively). This amount is not unusual when compared to the local climatology of the period 1970−2020, as
shown in Fig 1. The average locally-measured height of the lowest cloud base (i.e. vertical visibility) was roughly 1.2 km, and
130 the total cloudiness was determined to be on average 5 oktas. Details of the local monthly weather parameters from February
2019 to April 2020 can be found in Fig. A1.

3 Results and discussion

3.1 Snowfall events and coinciding vertical atmospheric profiles

We analysed a total of 468 radiosonde profiles that coincided with the MASC instrument being operational (i.e. eight months
135 of two winter seasons). Radiosondes were launched at 11:30 and 23:30 UTC. Ice particles captured by the camera and recorded
within the 15 minutes prior to each radiosonde launch were considered as coincident, although the path of the radiosondes is
not exactly the same as that of the recorded ice particles. The time span of 15 minutes was chosen for practical reasons so that
even during low precipitation intensity several ice particles were recorded. Three coinciding observations were not included in
our analysis, as it was either raining (10 Feb 2020 at 11:30 and 23:30 UTC) or snow was likely blowing off the ground during
140 unusually strong winds (30 Mar 2019 at 11:30 UTC). A minimum of 10 images with ice particles of $\geq$ 0.54 mm^2 in size within
these 15-minute intervals before each radiosonde launch is the criterion for what we consider a snowfall event. Instances with
less than 10 such images are considered "no-snowfall".

A snowfall event therefore corresponds to a minimum precipitation intensity of about 0.01 mm h^{-1} (assuming spherical ice
particles with 0.4 mm radius). The maximum and median number of images with objects larger than 0.54 mm^2 per snowfall
145 event were 630 and 68, respectively (Fig. A3). Consequently, the median concentration of such objects in the precipitating air
column would have been around 76 m^{-3}, assuming an average fall speed of 1 m s^{-1} (i.e. Locatelli and Hobbs, 1974). A total of
7401 objects were detected on MASC images coinciding with the radiosonde profiles. More than half of these objects (57%)
were blurred, dark, or not entirely visible on the pre-defined image selection. The remaining (3156) were analysed for their size
and visually for ice particle class, eventual riming, and aggregation. These analysed objects had mean and median projected
150 areas of 1.8 mm^2 and 1.1 mm^2, respectively (Fig. 2).

Out of 468 radiosonde profiles coinciding with the MASC instrument being operational, 62 were classified as snowfall events and the rest were considered no-snowfall (Fig. A3). For each 15-min event, meteorological parameters on ground were calculated from two weighed 10-min resolved data points and summarised (Fig. 3). During snowfall, the median and maximum wind speeds at 22 m above ground were 2.3 m s^{-1} and 4.2 m s^{-1}, respectively, and the median air temperature was

155 -2.3 °C. This is consistent with the results of Kochendorfer et al. (2017) for precipitation periods in the winter seasons of the time period 2013$-$2015. Moreover, during snowfall events, the median wind at 22 m above ground was from the East (96 °) although at greater altitude (2.7 km) it was mostly from West to Southwest (Fig. A2) and the median precipitation rate was relatively low with 0.15 mm h^{-1}, as determined optically with the Parsivel^2. Somewhat higher values were measured with the Pluvio^2 (0.24 mm h^{-1}). During snowfall, the visibility was on average 2020 m, the average base height of the lowest cloud

160 was 213 m, the sky was fully cloud covered (cloud cover = 8) and it was slightly snowing (code of "present weather" = 71). This suggests that snowfall was produced by stratiform clouds almost touching ground level. For events without snowfall, the median precipitation rate was zero, regardless of the measurement technique. The comparison of various other meteorological parameters between events with and without snowfall showed that some parameters differed in terms of range and median (i.e. relative humidity, pressure, wind direction, visibility, first cloud base height, cloudiness, and present weather). Other parameters

165 were relatively similar during snowfall as during no-snowfall events (i.e. air temperature, snow depths, and wind speed).

The relative humidity with respect to ice (RH$_{ice}$) of the profiles during snowfall showed a consistent pattern (Fig. 4a). RH$_{ice}$ was close to saturation at ground, increased slightly within the first few hundred metres, and remained above and close to 100% RH$_{ice}$ in the lower troposphere up to roughly 3 km. Above this altitude, RH$_{ice}$ values were more scattered among the profiles, with some profiles showing supersaturation with respect to ice up to 10 km. Consistently during snowfall, the relative humidity

170 profiles with respect to water (RH$_{water}$) showed values close to 100% from ground to a few hundreds of meters, followed by a slight decrease with increasing altitude up to 3 km, and a stronger variation above this altitude (Fig. A4a). RH$_{ice}$ and RH$_{water}$ of the profiles not associated with solid precipitation showed no such consistent pattern (Fig. 4b and Fig. A4b).

3.2 Necessary or sufficient RH$_{ice}$ conditions for snowfall

To test whether RH$_{ice}$ close to saturation throughout the lower $\sim$ 3 km of the atmosphere is a necessary or sufficient con-

175 dition for snowfall at the site, we evaluated a range of RH$_{ice}$ values and altitude ranges using different metrics, including accuracy (ACC), critical success index (CSI), and Heidke skill score (HSS), as shown in Fig. 5. An overview of the indices can be found in the Appendix (Table A1). All three indices have an optimal value of 1, favour hits, and penalise both misses and false alarms. Based on the results of three indices, the best scores were obtained for the following combination of values (from hereon: criterion): running mean RH$_{ice} \geq 97\%$ throughout the lower 2.7 km of the atmosphere. Choosing different values for

180 running mean RH$_{ice}$ and altitude reduced the overall accuracy of the prediction of snowfall events, although a running mean RH$_{ice} \geq 96\%$ throughout the lower 2.7 km of the atmosphere also yielded a very good score.

Of the total of 468 radiosonde profiles, 64 met the criterion of a running mean RH$_{ice} \geq 97\%$ throughout the lower 2.7 km (Fig. 6). In 81% of them (52 of 64) snowfall was observed (*hits*). In 10 cases the criterion was not met but snowfall was observed (*misses*). In 12 cases the criterion was met but no snowfall was observed (*false alarms*) and in 394 cases the criterion

185 was not met and no snowfall was observed (*correct negatives*). In other words, these specific thresholds of RH_{ice} and altitude correctly predicted 84% (52 of 62) and 97% (394 of 406) of the cases with and without snowfall, respectively. Although the criterion of a running mean $RH_{ice} \geq 97\%$ throughout the lower 2.7 km was neither absolutely necessary nor sufficient for snowfall to occur, it still separates the majority of snowfall events from no-snowfall events and vice versa.

3.3 Snowfall rate and type

190 In this section we will focus on the 52 snowfall events coinciding with a running mean $RH_{ice} \geq 97\%$ throughout the lower 2.7 km (i.e. *hits*, Fig. 6a), which seem to represent the predominant condition in which snowfall occurs in Northern Finland. These events were associated with optically measured median and maximum snowfall rates of 0.18 mm h^{-1} and 1.03 mm h^{-1}, respectively, as derived from the Parsivel[2] precipitation measurements. Only four of them were associated with snowfall rates <0.05 mm h^{-1} (Fig. A6a). In general, the snowfall rates for the 52 snowfall events we now consider were significantly higher

195 than for the other cases (i.e. *misses*, *false alarms* and *correct negatives* (see Fig. 6b-d), as shown in Fig. A6.

Excluding the invalid objects (i.e. blurred or dark), a total of 2853 analysed ice particles were captured during these 52 snowfall events. They had a median projected area of around 1.1 mm^2 (not shown) and a very similar size distribution to that of all events, which are shown in Fig. 2. Many of these objects on the visually inspected images had undefinable habits. Only 29% of them (827 of 2835) could unequivocally be classified by their habit. Nine different unequivocal crystal habits were

200 observed (Fig. 7a). The majority of them were single ice crystals and unrimed (Fig. 7b). Most ice crystals had habits that form below liquid water saturation (i.e. single plates, columns, radiating plates, rosettes, or their aggregates). Notably, the shapes that grow below the liquid water saturation were often unrimed (not shown). The most common habit of the classifiable ice particles was radiating plates, with a share of 54% (447 of 827).

3.4 Properties of ice crystals and air masses related to maximum RH_{water} along the profile

205 We grouped the 52 snowfall events under consideration according to their maximum running mean RH_{water} along the radiosonde profiles into three similarly large sub-groups: < 98% (n = 18), $\geq$ 98% and < 99% (n = 20), and $\geq$ 99% (n = 14), as shown in Fig. 8a-c. For each sub-group, we determined the corresponding ice particle size distribution and ice particle classes (Fig. 8d-i). Overall, 14 of 52 events (27%) reached a maximum running mean RH_{water} along the profile between 99% and 100% (Fig. 8c). These events coincided with ice particles that were (1) larger (Fig. 8f), (2) more often rimed and aggregated, and (3) more

210 often associated with habits that grow above the water saturation line (i.e. needles, graupel, spatial dendrites, dendrites, and stellar plates; Fig. 8i) as compared to those events (38 of 52) that did not reach a maximum running mean RH_{water} of 99% (Fig. 8a,b,d,e,g,h). Hence, only around one quarter of all precipitating clouds seem to have been mixed-phase and the rest were probably fully glaciated. The lowest proportion of riming and aggregation was found for events for which the maximum running mean RH_{water} did not exceed 98% (Fig. 8a,d,g). These results suggest that the humidity measurements by the radiosondes during

215 our measurement campaign and in the lower 3 km of the atmosphere were more accurate near saturation with respect to water than the 4% promised by the manufacturer, at least when averaged over 500 m.

Most air masses associated with the 52 snowfall events tended to come from a southerly to westerly direction and crossed marine areas shortly before arriving at the site (Fig. 9 and Fig. A2b), which suggests that the Baltic Sea, the Norwegian Sea and the North Sea were the major sources of moisture for snowfall in the observed cases. The few air masses that did not

220 pass over marine areas recently, but crossed Russia and Eastern Europe, were associated with maximum running mean RH_{water} below 99%.

3.5 Likely underlying ice formation processes

To determine whether heterogeneous or homogeneous freezing might have triggered the initial ice formation during the considered 52 snowfall events (coinciding with running mean $RH_{ice} \geq 97\%$ throughout the lower 2.7 km), we extracted from the

225 radiosonde profiles the likely cloud top temperature, which is the temperature at which initial ice might have formed. Since a higher level cloud could seed a lower level cloud (e.g. Vassel et al., 2019; Ramelli et al., 2021; Proske et al., 2021), we determined the cloud top of the highest possible seeding cloud by assuming differently-sized gaps that ice crystals could potentially pass without complete sublimation. Depending on the assumed width of the gap between potential seeder and feeder clouds (i.e. ≤ 0.2 km, ≤ 0.5 km, or ≤ 1 km), between 30% and 75% of the cloud tops were colder than $-38\,°C$ (Fig. 10a).

230 Here, freezing would have been initiated via homogeneous freezing (Murray et al., 2010). However, between 25% and 60% of the cloud tops may have had temperatures warmer than $-38\,°C$. In these cases, ice formation would have been initiated via heterogeneous freezing. Since RH_{ice} and RH_{water} along the profiles were often $< 130\%$ and $< 100\%$, respectively (i.e. Figs. 4a and 8a-c), it could be that initial ice formed via pore condensation and freezing onto mineral dust, biogenic particles or other ice-nucleating particles (INPs) (Kanji and Abbatt, 2006; David et al., 2019).

235 We may estimate whether enough INPs were present to explain the number of ice particles observed by using the empirical parameterisation by Schneider et al. (2021):

$$INP\left(T\right) = 0.1 \cdot exp\left(a1 \cdot T_{amb} + a2\right) \cdot exp\left(b1 \cdot T + b2\right) stdL^{-1} \tag{1}$$

where $INP\left(T\right)$ is the number concentration of INPs (in $stdL^{-1}$) active at temperature T (in K), T_{amb} is the ambient air temperature at ground level (in K), and $a1$, $a2$, $b1$, and $b2$ are empirically fitted parameters ($a1 = 0.074$ K^{-1}, $a2 = -18$, $b1$

240 $= -0.504$ K^{-1}, $b2 = 127$). For each event we used daily averaged local temperatures for T_{amb} to calculate the INP number concentration active at cloud top temperatures. Median INP concentrations were 19 m^{-3}, 79 m^{-3}, and 5054 m^{-3}, respectively, depending on the assumed gap-width between potential seeder and feeder clouds (Fig. 10b). Such INP concentrations are within the range of observed long-term median INP concentrations active between $-20\,°C$ (60 m^{-3}) and $-30\,°C$ (690 m^{-3}) in condensation mode (i.e. $RH_{water} = 101\%$) at an Arctic site in Svalbard (474 m a.s.l.; Schrod et al., 2020). For an assumed

245 gap-width between potential seeder and feeder clouds of 0.5 km and 1 km the number of estimated INPs would have been sufficient to generate the observed ice particles. For a narrower gap-width (0.2 km), a multiplication factor of 3 would need to be invoked to explain the observations. Therefore, secondary ice formation processes were probably not of much relevance, although we saw some broken-off branches of dendrites, suggesting at least occasional ice–ice collision followed by breakup

(i.e. Vardiman, 1978). This secondary ice mechanism was shown to be linked to the collision force and the riming degree,

250 with a number of observed fragments per collision below 1 for unrimed dendrites and below 8 for lightly rimed dendrites (Vardiman, 1978; Phillips et al., 2017). Other secondary ice mechanism, such as rime-splintering (e.g. Hallett and Mossop, 1974) and droplet fragmentation (e.g. Takahashi and Yamashita, 1970), would require the presence of liquid droplets, which seem to have been rare during our observations.

4   Conclusions

255 Overall, about 70% of all classifiable ice crystals observed during the 52 snowfall events (i.e. events that had a minimum of 10 images with ice particles of ≥ 0.54 mm^2 in size within 15-minute intervals) that were correctly predicted using our basic RH$_{ice}$ criteria (i.e. running mean RH$_{ice} \geq 97\%$ throughout the lower 2.7 km) in Northern Finland had habits that form below the water saturation. In a similar proportion of radiosonde profiles, the running mean RH$_{water}$ did not reach values $\geq 99\%$. This suggests that snowfall in this region was derived from ice clouds in nearly three quarters of the cases. As ice particles grow very slowly

260 in such conditions, the lower atmosphere can not be much below saturation with respect to ice for snowfall to occur. Otherwise, the small, often unrimed ice particles would not reach the surface before completely sublimating. These precipitating clouds are probably stratiform clouds that extend from close to the ground to at least 2.7 km altitude. At that altitude the air masses arrived mostly from West and Southwest. Probably, the Baltic Sea, the Norwegian Sea, and the North Sea were the major source of moisture generating snowfall in Northern Finland. Due to orographic lifting at the coastal mountain range, North

265 Atlantic air masses might already have lost much of their initial moisture content when arriving in Northern Finland.

In a warmer climate, the partitioning of ice particles and liquid cloud droplets in Arctic clouds may shift in favour of liquid droplets. Therefore, a greater proportion of mixed-phase clouds than currently observed can be expected. Such microphysical changes depend on the availability of INPs, which are currently responsible for perhaps half of the initial ice formation and would affect cloud properties, such as radiation and precipitation. In the future, the effects of eventual changes in predomi-

270 nant cloud phase should be further investigated through measurements of ice crystal habits, INPs, precipitation, and radiation properties to better understand potential feedback mechanisms between climate change and cloud properties.

Data availability.   The RS41 GRUAN data products are available via https://www.gruan.org/instruments/radiosondes/sonde-models/vaisa la-rs41 (last access: 31 January 2022). The ground-based weather parameters are accessible via https://litdb.fmi.fi/luo0015_data.php (last access: 31 January 2022). The MASC images and the code are available from the authors upon request.

275 *Author contributions.*   CM and FC conceived the study. LZ modified, installed and maintained the MASC instrument with help from FC and know-how from AB. RK performed the radiosonde launches. LZ processed the MASC images and CM classified the ice particles. CM performed the analysis and prepared the figures. CM, LZ, RK, AB and FC interpreted the data. CM drafted the manuscript with contributions from all co-authors.

Competing interests. The authors declare that they have no conflict of interest.

280 *Acknowledgements.* The authors are grateful to the Finnish Meteorological Institute for providing the infrastructure as well as the ground-based weather parameters on site. We thank the team in Sodankylä for their support on site. Special thanks to Jaakko Siltakoski for providing images of the MASC instrument and helping during the installations in the SPICE field. We greatly appreciate the support of Antti Poikonen for establishing remote access to the MASC and Michael Sommer for his help in downloading the GRUAN data. We are grateful to Pedro Batista for his advice during coding in R and his help in creating the maps in GIS. We acknowledge the NOAA Air Resources Laboratory for

285 providing access to the HYSPLIT model through the READY website (https://www.ready.noaa.gov/HYSPLIT.php, last access: 31 January 2022). We acknowledge financial support by the Swiss National Science Foundation as well as the Department of Environmental Sciences at University of Basel.

Financial support. This study has been supported by Swiss National Science Foundation (grant number 200021_169620) and the Department of Environmental Sciences, University of Basel.

References

Bailey, M. P. and Hallett, J.: A comprehensive habit diagram for atmospheric ice crystals: confirmation from the laboratory, AIRS II, and other field studies, J. Atmos. Sci., 66, 2888–2899, https://doi.org/10.1175/2009JAS2883.1, 2009.

Barnett, T., Adam, J., and Lettenmaier, D.: Potential impacts of a warming climate on water availability in snow-dominated regions, Nature, 438, 303–309, https://doi.org/10.1038/nature04141, 2005.

Bennett, N. D., Croke, B. F., Guariso, G., Guillaume, J. H., Hamilton, S. H., Jakeman, A. J., Marsili-Libelli, S., Newham, L. T., Norton, J. P., Perrin, C., Pierce, S. A., Robson, B., Seppelt, R., Voinov, A. A., Fath, B. D., and Andreassian, V.: Characterising performance of environmental models, Environ. Modell. Softw., 40, 1–20, https://doi.org/10.1016/j.envsoft.2012.09.011, 2013.

Boudala, F. S., Isaac, G. A., Rasmussen, R., Cober, S. G., and Scott, B.: Comparisons of Snowfall Measurements in Complex Terrain Made During the 2010 Winter Olympics in Vancouver, Pure Appl. Geophys., 171, 113–127, https://doi.org/10.1007/s00024-012-0610-5, 2014.

Casella, D., Panegrossi, G., Sanò, P., Marra, A. C., Dietrich, S., Johnson, B. T., and Kulie, M. S.: Evaluation of the GPM-DPR snowfall detection capability: Comparison with CloudSat-CPR, Atmospheric Research, 197, 64–75, https://doi.org/10.1016/j.atmosres.2017.06.018, 2017.

Costa, A., Meyer, J., Afchine, A., Luebke, A., Günther, G., Dorsey, J. R., Gallagher, M. W., Ehrlich, A., Wendisch, M., Baumgardner, D., Wex, H., and Krämer, M.: Classification of Arctic, midlatitude and tropical clouds in the mixed-phase temperature regime, Atmos. Chem. Phys., 17, 12 219–12 238, https://doi.org/10.5194/acp-17-12219-2017, 2017.

David, R. O., Marcolli, C., Fahrni, J., Qiu, Y., Perez Sirkin, Y. A., Molinero, V., Mahrt, F., Brühwiler, D., Lohmann, U., and Kanji, Z. A.: Pore condensation and freezing is responsible for ice formation below water saturation for porous particles, Proceedings of the National Academy of Sciences, 116, 8184–8189, https://doi.org/10.1073/pnas.1813647116, 2019.

Delanoë, J., Protat, A., Jourdan, O., Pelon, J., Papazzoni, M., Dupuy, R., Gayet, J.-F., and Jouan, C.: Comparison of airborne in situ, airborne Radar–Lidar, and spaceborne Radar–Lidar retrievals of polar ice cloud properties sampled during the POLARCAT campaign, J. Atmos. Ocean. Technol., 30, 57 – 73, https://doi.org/10.1175/JTECH-D-11-00200.1, 2013.

Fick, S. E. and Hijmans, R. J.: WorldClim 2: new 1-km spatial resolution climate surfaces for global land areas, Int. J. Climatol., 37, 4302–4315, https://doi.org/10.1002/joc.5086, 2017.

Fridlind, A. M., van Diedenhoven, B., Ackerman, A. S., Avramov, A., Mrowiec, A., Morrison, H., Zuidema, P., and Shupe, M. D.: A FIRE-ACE/SHEBA case study of mixed-phase Arctic boundary layer clouds: Entrainment rate limitations on rapid primary ice nucleation processes, J. Atmos. Sci., 69, 365–389, https://doi.org/10.1175/JAS-D-11-052.1, 2012.

Fukuta, N. and Takahashi, T.: The growth of atmospheric ice crystals: A summary of findings in vertical supercooled cloud tunnel studies, J. Atmos. Sci., 56, 1963–1979, 1999.

Garrett, T., Fallgatter, C., Shkurko, K., and Howlett, D.: Fall speed measurement and high-resolution multi-angle photography of hydrometeors in free fall, Atmos. Meas. Tech., 5, 2625–2633, 2012.

Gierens, R., Kneifel, S., Shupe, M. D., Ebell, K., Maturilli, M., and Löhnert, U.: Low-level mixed-phase clouds in a complex Arctic environment, Atmos. Chem. Phys., 20, 3459–3481, https://doi.org/10.5194/acp-20-3459-2020, 2020.

Hall, A. and Qu, X.: Using the current seasonal cycle to constrain snow albedo feedback in future climate change, Geophys., 33, https://doi.org/10.1029/2005GL025127, 2006.

Hallett, J. and Mossop, S. C.: Production of secondary ice particles during the riming process, Nature, 249, 26–28, 1974.

Hanna, J. W., Schultz, D. M., and Irving, A. R.: Cloud-top temperatures for precipitating winter clouds, J. Appl. Meteorol. Climatol., 47, 351—359, https://doi.org/10.1175/2007JAMC1549.1, 2008.

Hirsikko, A., O'Connor, E. J., Komppula, M., Korhonen, K., Pfüller, A., Giannakaki, E., Wood, C. R., Bauer-Pfundstein, M., Poikonen, A., Karppinen, T., Lonka, H., Kurri, M., Heinonen, J., Moisseev, D., Asmi, E., Aaltonen, V., Nordbo, A., Rodriguez, E., Lihavainen, H.,
330   Laaksonen, A., Lehtinen, K. E. J., Laurila, T., Petäjä, T., Kulmala, M., and Viisanen, Y.: Observing wind, aerosol particles, cloud and precipitation: Finland's new ground-based remote-sensing network, Atmos. Meas. Tech., 7, 1351–1375, https://doi.org/10.5194/amt-7-1351-2014, 2014.

Hobbs, P. V., Chang, S., and Locatelli, J. D.: The dimensions and aggregation of ice crystals in natural clouds, J. Geophys. Res., 79, 2199–.2206, https://doi.org/10.1029/JC079i015p02199, 1974.

335   Hyvärinen, O.: A Probabilistic Derivation of Heidke Skill Score, Weather Forecast., 29, 177 – 181, https://doi.org/10.1175/WAF-D-13-00103.1, 2014.

Jensen, M. P., Holdridge, D. J., Survo, P., Lehtinen, R., Baxter, S., Toto, T., and Johnson, K. L.: Comparison of Vaisala radiosondes RS41 and RS92 at the ARM Southern Great Plains site, Atmos. Meas. Tech., 9, 3115–3129, https://doi.org/10.5194/amt-9-3115-2016, 2016.

Jiusto, J. E. and Weickmann, H. K.: types of snowfall, Bull. Am. Meteorol. Soc., 54, 1148 – 1162, https://doi.org/10.1175/1520-
340   0477(1973)054<1148:TOS>2.0.CO;2, 1973.

Kanji, Z. A. and Abbatt, J. P. D.: Laboratory studies of ice formation via deposition mode nucleation onto mineral dust and n-hexane soot samples, J. Geophys., 111, https://doi.org/10.1029/2005JD006766, 2006.

Kanji, Z. A., Ladino, L. A., Wex, H., Boose, Y., Burkert-Kohn, M., Cziczo, D. J., and Krämer, M.: Overview of ice nucleating particles, Meteor. Mon., 58, 1.1–1.33, https://doi.org/10.1175/AMSMONOGRAPHS-D-16-0006.1, 2017.

345   Kikuchi, M., Okamoto, H., Sato, K., Suzuki, K., Cesana, G., Hagihara, Y., Takahashi, N., Hayasaka, T., and Oki, R.: Development of algorithm for discriminating hydrometeor particle types with a synergistic use of CloudSat and CALIPSO, J. Geophys., 122, 11,022–11,044, https://doi.org/10.1002/2017JD027113, 2017.

Kneifel, S. and Moisseev, D.: Long-term statistics of riming in nonconvective clouds derived from ground-based Doppler cloud radar observations, J. Atmos. Sci., 77, 3495 – 3508, https://doi.org/10.1175/JAS-D-20-0007.1, 2020.

350   Kobayashi, T.: The growth of snow crystals at low supersaturations, Philosophical Magazine, 6, 1363–1370, https://doi.org/10.1080/14786436108241231, 1961.

Kochendorfer, J., Nitu, R., Wolff, M., Mekis, E., Rasmussen, R., Baker, B., Earle, M. E., Reverdin, A., Wong, K., Smith, C. D., Yang, D., Roulet, Y.-A., Buisan, S., Laine, T., Lee, G., Aceituno, J. L. C., Alastrué, J., Isaksen, K., Meyers, T., Brækkan, R., Landolt, S., Jachcik, A., and Poikonen, A.: Analysis of single-Alter-shielded and unshielded measurements of mixed and solid precipitation from WMO-SPICE,
355   Hydrol. Earth. Syst. Sci., 21, 3525–3542, https://doi.org/10.5194/hess-21-3525-2017, 2017.

Liu, G.: Deriving snow cloud characteristics from CloudSat observations, J. Geophys., 113, https://doi.org/10.1029/2007JD009766, 2008.

Locatelli, J. D. and Hobbs, P. V.: Fall speeds and masses of solid precipitation particles, J. Geophys., 79, 2185–2197, 1974.

Madonna, F., Kivi, R., Dupont, J.-C., Ingleby, B., Fujiwara, M., Romanens, G., Hernandez, M., Calbet, X., Rosoldi, M., Giunta, A., Karppinen, T., Iwabuchi, M., Hoshino, S., von Rohden, C., and Thorne, P. W.: Use of automatic radiosonde launchers to measure temperature
360   and humidity profiles from the GRUAN perspective, Atmos. Meas. Tech., 13, 3621–3649, https://doi.org/10.5194/amt-13-3621-2020, 2020.

Magono, C. and Lee, C. W.: Meteorological classification of natural snow crystals, Journal of the Faculty of Science, Hokkaido University, Series 7, 2, 321–335, 1966.

Mioche, G., Jourdan, O., Delanoë, J., Gourbeyre, C., Febvre, G., Dupuy, R., Monier, M., Szczap, F., Schwarzenboeck, A., and Gayet, J.-F.: Vertical distribution of microphysical properties of Arctic springtime low-level mixed-phase clouds over the Greenland and Norwegian seas, Atmos. Chem. Phys., 17, 12 845–12 869, https://doi.org/10.5194/acp-17-12845-2017, 2017.

Morrison, H., Zuidema, P., McFarquhar, G. M., Bansemer, A., and Heymsfield, A. J.: Snow microphysical observations in shallow mixed-phase and deep frontal Arctic cloud systems, Q. J. R. Meteorol. Soc., 137, 1589–1601, https://doi.org/10.1002/qj.840, 2011.

Mosimann, L., Weingartner, E., and Waldvogel, A.: An Analysis of Accreted Drop Sizes and Mass on Rimed Snow Crystals, J. Atmos. Sci., 51, 1548 – 1558, https://doi.org/10.1175/1520-0469(1994)051<1548:AAOADS>2.0.CO;2, 1994.

Mossop, S. C.: The influence of drop size distribution on the production of secondary ice particles during graupel growth, Q. J. Roy. Meteor. Soc., 104, 323–330, https://doi.org/10.1002/qj.49710444007, 1978.

Murray, B. J., Broadley, S. L., Wilson, T. W., Bull, S. J., Wills, R. H., Christenson, H. K., and Murray, E. J.: Kinetics of the homogeneous freezing of water, Phys, Chem. Chem. Phys., 12, 10 380–10 387, https://doi.org/10.1039/c003297b, 2010.

Mülmenstädt, J., Sourdeval, O., Delanoë, J., and Quaas, J.: Frequency of occurrence of rain from liquid-, mixed-, and ice-phase clouds derived from A-Train satellite retrievals, Geophys. Res. Lett., 42, 6502–6509, https://doi.org/10.1002/2015GL064604, 2015.

Nakaya, U.: Snow crystals: Natural and artificial, Harvard University Press, Cambridge, UK, 510 pp., 1954.

Nelson, J. T. and Baker, M. B.: New theoretical framework for studies of vapor growth and sublimation of small ice crystals in the atmosphere, J. Geophys. Res., 101, 7033–7047, https://doi.org/10.1029/95JD03162, 1996.

Nitu, R., Roulet, Y.-A., Wolff, M., Earle, M., Reverdin, A., Smith, C., Kochendorfer, J., Morin, S., Rasmussen, R., Wong, K., Alastrué, J., Arnold, L., Baker, B., Buisán, S., Collado, J., Colli, M., Collins, B., Gaydos, A., Hannula, H.-R., Hoover, J., Joe, P., Kontu, A., Laine, T., Lanza, L., Lanzinger, E., Lee, G., Lejeune, Y., Leppänen, L., Mekis, E., Panel, J.-M., Poikonen, A., Ryu, S., Sabatini, F., Theriault, J., Yang, D., Genthon, C. van den Heuvel, F., Hirasawa, N., Konishi, H., Motoyoshi, H., Nakai, S., Nishimura, K., Senese, A., and Yamashita, K.: WMO Solid Precipitation Intercomparison Experiment (SPICE) (2012–2015), IOM Report No. 131, https://library.wmo.int/index.php?lvl=notice_display&id=20742, 2018.

Phillips, V. T. J., Yano, J.-I., and Khain, A.: Ice multiplication by breakup in ice-ice collisions. Part I: Theoretical formulation, J. Atmos. Sci., 74, 1705–1719, https://doi.org/10.1175/JAS-D-16-0224.1, 2017.

Power, B. A., Summers, P. W., and D'Avignon, J.: Snow crystal forms and riming effects as related to snowfall density and general storm conditions, J. Atmos. Sci., 21, 300 – 305, https://doi.org/10.1175/1520-0469(1964)021<0300:SCFARE>2.0.CO;2, 1964.

Praz, C., Roulet, Y.-A., and Berne, A.: Solid hydrometeor classification and riming degree estimation from pictures collected with a Multi-Angle Snowflake Camera, Atmos. Meas. Tech., 10, 1335–1357, https://doi.org/10.5194/amt-10-1335-2017, 2017.

Proske, U., Bessenbacher, V., Dedekind, Z., Lohmann, U., and Neubauer, D.: How frequent is natural cloud seeding from ice cloud layers ($< -35\,°C$) over Switzerland?, Atmos. Chem. Phys., 21, 5195–5216, https://doi.org/10.5194/acp-21-5195-2021, 2021.

Ramelli, F., Henneberger, J., David, R. O., Bühl, J., Radenz, M., Seifert, P., Wieder, J., Lauber, A., Pasquier, J. T., Engelmann, R., Mignani, C., Hervo, M., and Lohmann, U.: Microphysical investigation of the seeder and feeder region of an Alpine mixed-phase cloud, Atmos. Chem. Phys., 21, 6681–6706, https://doi.org/10.5194/acp-21-6681-2021, 2021.

Schneider, J., Höhler, K., Heikkilä, P., Keskinen, J., Bertozzi, B., Bogert, P., Schorr, T., Umo, N. S., Vogel, F., Brasseur, Z., Wu, Y., Hakala, S., Duplissy, J., Moisseev, D., Kulmala, M., Adams, M. P., Murray, B. J., Korhonen, K., Hao, L., Thomson, E. S., Castarède, D., Leisner, T., Petäjä, T., and Möhler, O.: The seasonal cycle of ice-nucleating particles linked to the abundance of biogenic aerosol in boreal forests, Atmos. Meas. Tech., 21, 3899–3918, https://doi.org/10.5194/acp-21-3899-2021, 2021.

Schrod, J., Thomson, E. S., Weber, D., Kossmann, J., Pöhlker, C., Saturno, J., Ditas, F., Artaxo, P., Clouard, V., Saurel, J.-M., Ebert, M., Curtius, J., and Bingemer, H. G.: Long-term deposition and condensation ice-nucleating particle measurements from four stations across the globe, Atmos. Chem. Phys., 20, 15 983–16 006, https://doi.org/10.5194/acp-20-15983-2020, 2020.

Seo, W.-S., Eun, S.-H., Kim, B.-G., Ko, A.-R., Seong, D.-K., Lee, K.-M., Jeon, H.-R., Han, S.-O., and Park, Y.-S.: Study on characteristics
405   of snowfall and snow crystal habits in the ESSAY (Experiment on Snow Storms At Yeongdong) campaign in 2014, Atmosphere, 25, 261–270, https://doi.org/10.14191/Atmos.2015.25.2.261, 2015.

Shupe, M. D. and Intrieri, J. M.: Cloud radiative forcing of the Arctic surface: The influence of cloud properties, surface albedo, and solar zenith angle, J. Clim., 17, 616 – 628, https://doi.org/10.1175/1520-0442(2004)017<0616:CRFOTA>2.0.CO;2, 2004.

Silber, I., Fridlind, A. M., Verlinde, J., Ackerman, A. S., Cesana, G. V., and Knopf, D. A.: The prevalence of precipitation from polar
410   supercooled clouds, Atmos. Chem. Phys., 21, 3949–3971, https://doi.org/10.5194/acp-21-3949-2021, 2021.

Takahashi, C. and Yamashita, A.: Shattering of frozen water drops in a supercooled cloud, J. Meteorol. Soc. Jpn., 48, 373–376, 1970.

Tan, I. and Storelvmo, T.: Evidence of strong contributions from mixed-phase clouds to Arctic climate change, Geophys. Res. Lett., 46, 2894–2902, https://doi.org/10.1029/2018GL081871, 2019.

Vardiman, L.: The generation of secondary ice particles in clouds by crystal—crystal collisions, J. Atmos. Sci., 35, 2168–2180,
415   https://doi.org/10.1175/1520-0469(1978)035<2168:TGOSIP>2.0.CO;2, 1978.

Vassel, M., Ickes, L., Maturilli, M., and Hoose, C.: Classification of Arctic multilayer clouds using radiosonde and radar data in Svalbard, Atmos. Chem. Phys., 19, 5111–5126, https://doi.org/10.5194/acp-19-5111-2019, 2019.
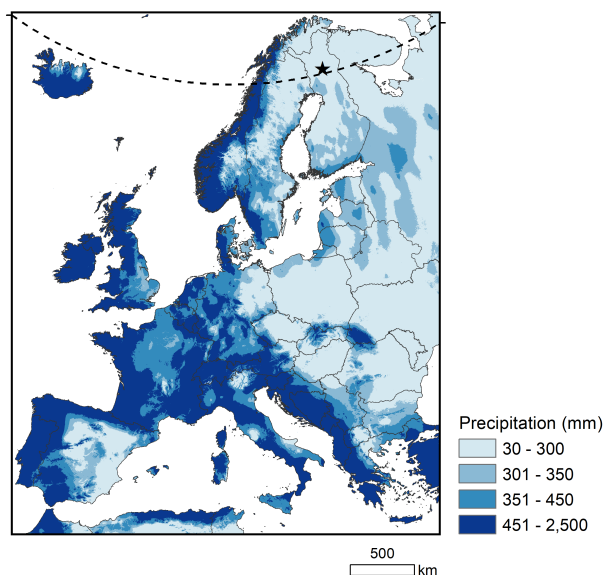
Figure 1. Overview of the geographical location of the experiment setup in Sodankylä, Finland (black star), located just above the Arctic Circle (dashed line). The average seven-month total precipitation (in mm) for the colder months per year (January-April and October-December) in the period 1970−2000 are shown in the map derived from the monthly climate data from WorldClim (Fick and Hijmans, 2017, see also https://www.worldclim.org/data/worldclim21.html, last access: 31 January 2022).
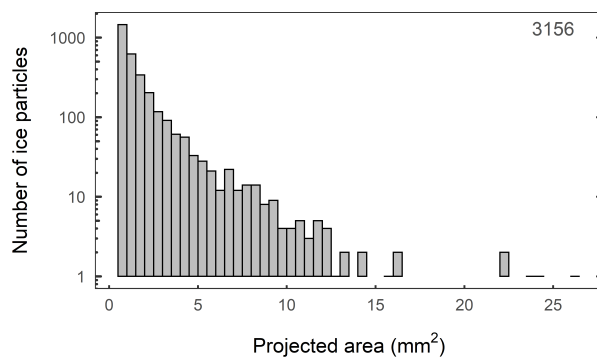
Figure 2. The number of analysed ice particles (n = 3156) by intervals of projected area (mm^2) roughly followed a power function. Analysed ice particles captured by the camera during the 15-min intervals prior to the radiosonde launches throughout the whole time span of interest (28 February 2019 to 7 April 2020) were considered.
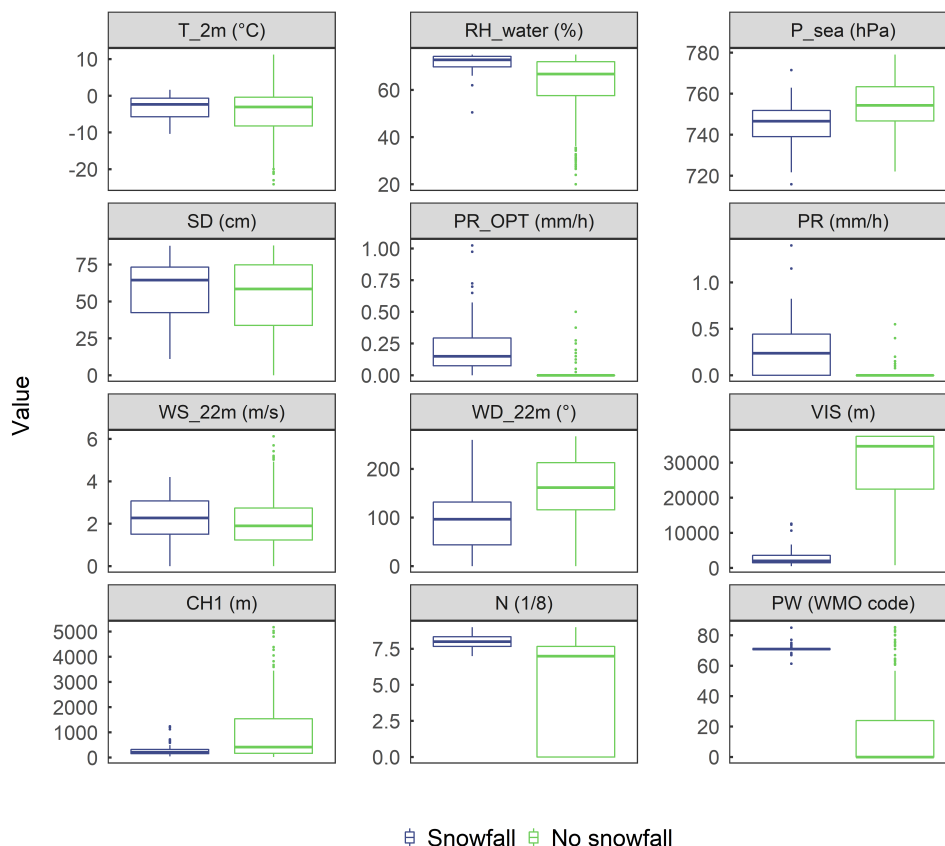
Figure 3. Boxplots (i.e. median (thick line), interquartile range (box), minima and maxima (whiskers), outliers (dots)) of weather parameters measured at the site coinciding with radiosonde profiles during events considered as snowfall (n = 62, blue) and as no-snowfall (n = 406, green). The following parameters are shown from the upper left to the bottom right: ambient air temperature at 2 m above ground (T_2m in °C), the relative humidity with respect to water (RH_water in %), the pressure at sea level (P_sea in hPa), the snow depth (SD in cm), the precipitation rate measured optically (PR_OPT in mm h^{-1}) and by weight (PR mm h^{-1}), the wind speed at 22 m above ground (WS_22m in m s^{-1}), the wind direction at 22 m above ground (WD_22m in °), the visibility (VIS in m), the height of the lowest cloud base (CH1 in m), the total cloudiness (N, a number between 1 (cloud free) and 8 (cloud covered)), and the present weather (PW using the WMO Code 4680).
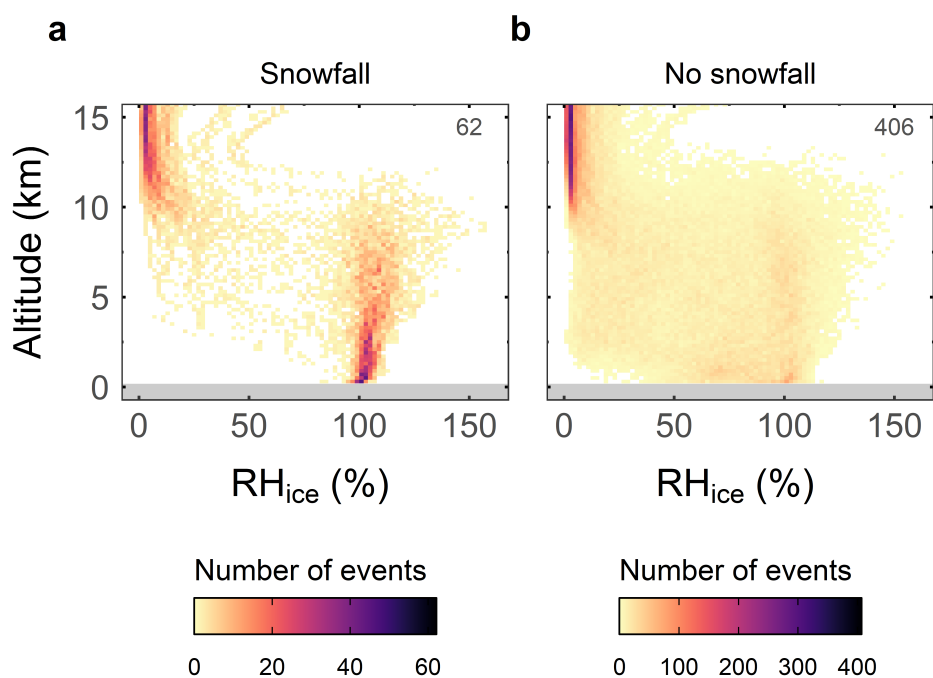
Figure 4. Relative humidity with respect to ice (RH_{ice}) within intervals of 200 m height and 2% RH_{ice} retrieved from the radiosonde profiles during (**a**) snowfall and (**b**) no-snowfall events. The total number of events for each group is provided in the upper right corner of each panel.
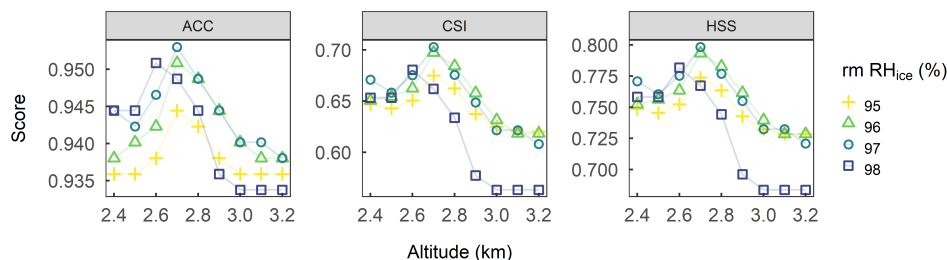
Figure 5. Scores to assess the prediction of snowfall using the running mean RH_{ice} values and altitude ranges were best for running mean $RH_{ice} \geq 97\%$ throughout the lower 2.7 km above ground. A set of different lower threshold values was investigated ranging for a running mean RH_{ice} from $\geq 95\%$ to $\geq 98\%$ throughout altitude ranges from ground level to between 2.4 km and 3.2 km above ground. Running means in RH_{ice} were calculated of five consecutive 100 m layers and the running mean was allocated to the lowest of the five layers. The following scores are shown: accuracy (ACC), critical success index (CSI), and Heidke skill score (HSS). See Table A1 for more information on the metrics.
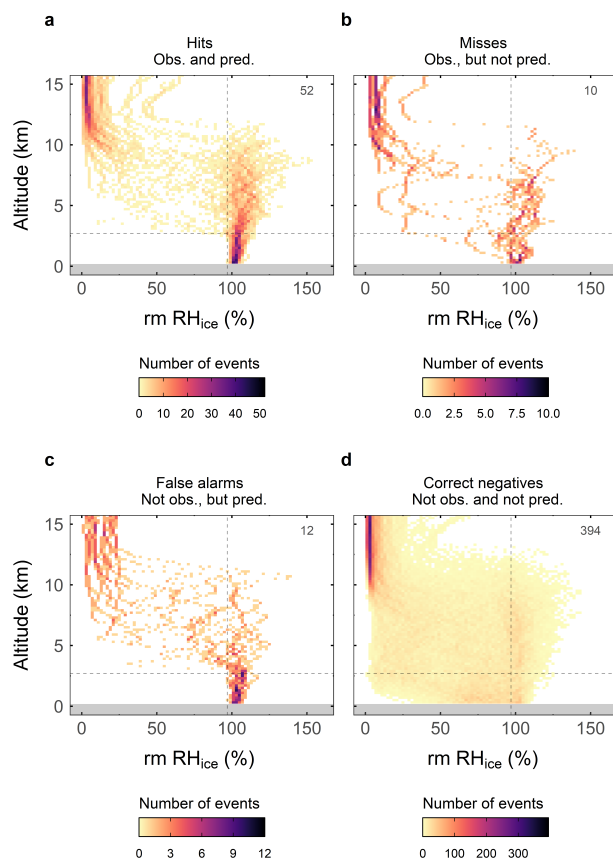
Figure 6. Observed values of running mean RH_{ice} binned in 200 m intervals and 2% steps of RH_{ice} for (**a**) *hits*, (**b**) *misses*, (**c**) *false alarms*, and (**d**) *correct negatives*. Snowfall was predicted for cases when running mean RH_{ice} measured along the radiosonde profile was $\geq 97\%$ (vertical dashed line) throughout the lower 2.7 km (horizontal dashed line) of the atmosphere. The total number of events per group is shown in the upper right corner of each panel.
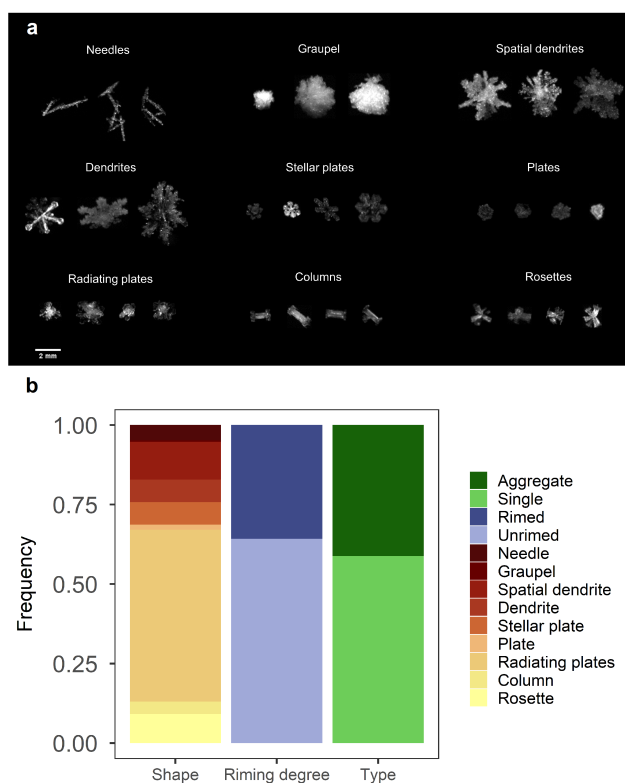
Figure 7. (**a**) Some examples of single, specifiable ice particles captured by the MASC and their shape. Of note, needles were only captured as aggregates. (**b**) Analysis of (827) unequivocal ice particles that were captured during the 52 snowfall events coinciding with a running mean $RH_{ice} \geq 97\%$ throughout the lower 2.7 km. Frequency with respect to shape (i.e. as shown in a), riming degree (i.e. unrimed or rimed) and type (i.e. single or aggregate) are shown.
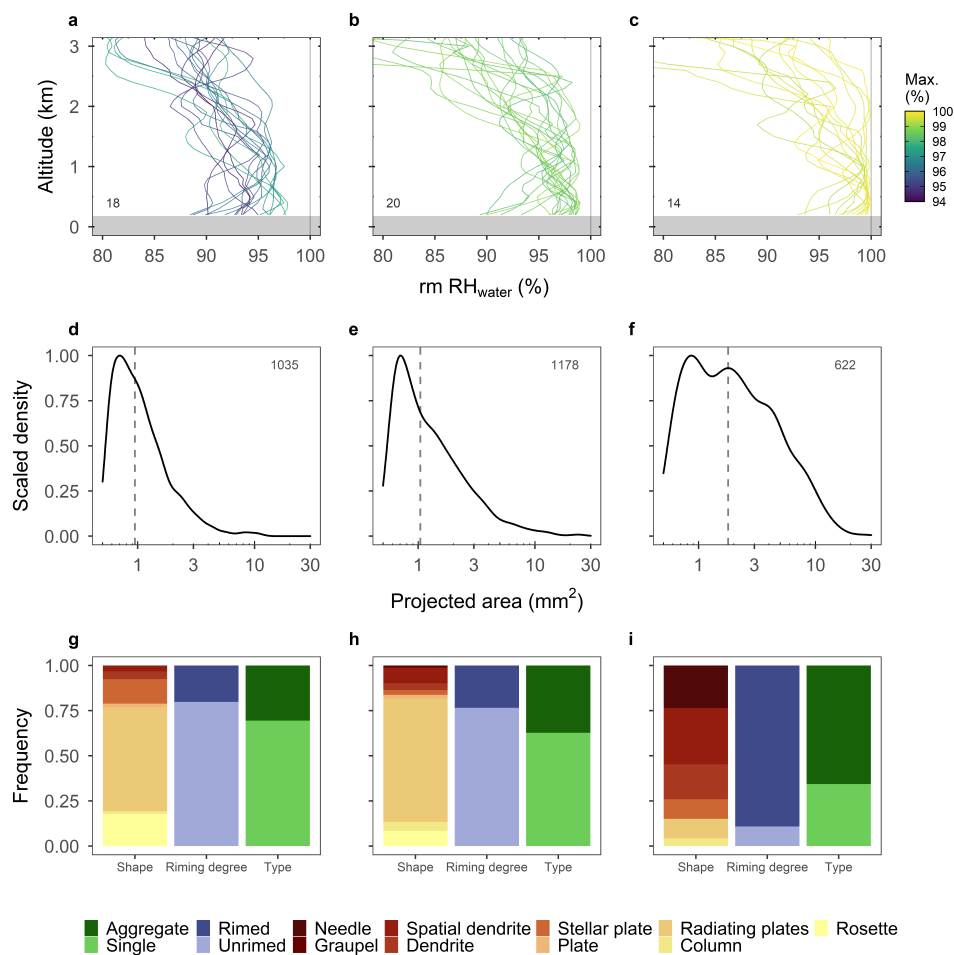
Figure 8. (**a, b, c**) Running mean RH$_{water}$ profiles coinciding with snowfall and running mean RH$_{ice} \geq 97\%$ throughout the lower 2.7 km (52 events) grouped by the maximum running mean RH$_{water}$. The maximum running mean RH$_{water}$ along the altitude profile is shown in colour. (**a**) Profiles with a maximum running mean RH$_{water} < 98\%$. (**b**) Profiles with a maximum running mean RH$_{water} \geq 98\%$ and $< 99\%$. (**c**) Profiles with a maximum running mean RH$_{water} \geq 99\%$. For each panel, the number of profiles is indicated in the left bottom corner. (**d, e, f**) The scaled density of ice particles by projected area (mm^2). All the analysed ice particles of the profiles in the above lying panel were considered. The dashed vertical line indicates the median area. The number of analysed ice particles is indicated by the number provided in the upper right corner. During the 52 snowfall events, a total of 2835 ice particles were analysed. (**g, h, i**) Same as Fig. 7b, but considering only the specifiable ice particles coinciding with the events of the above lying panels.
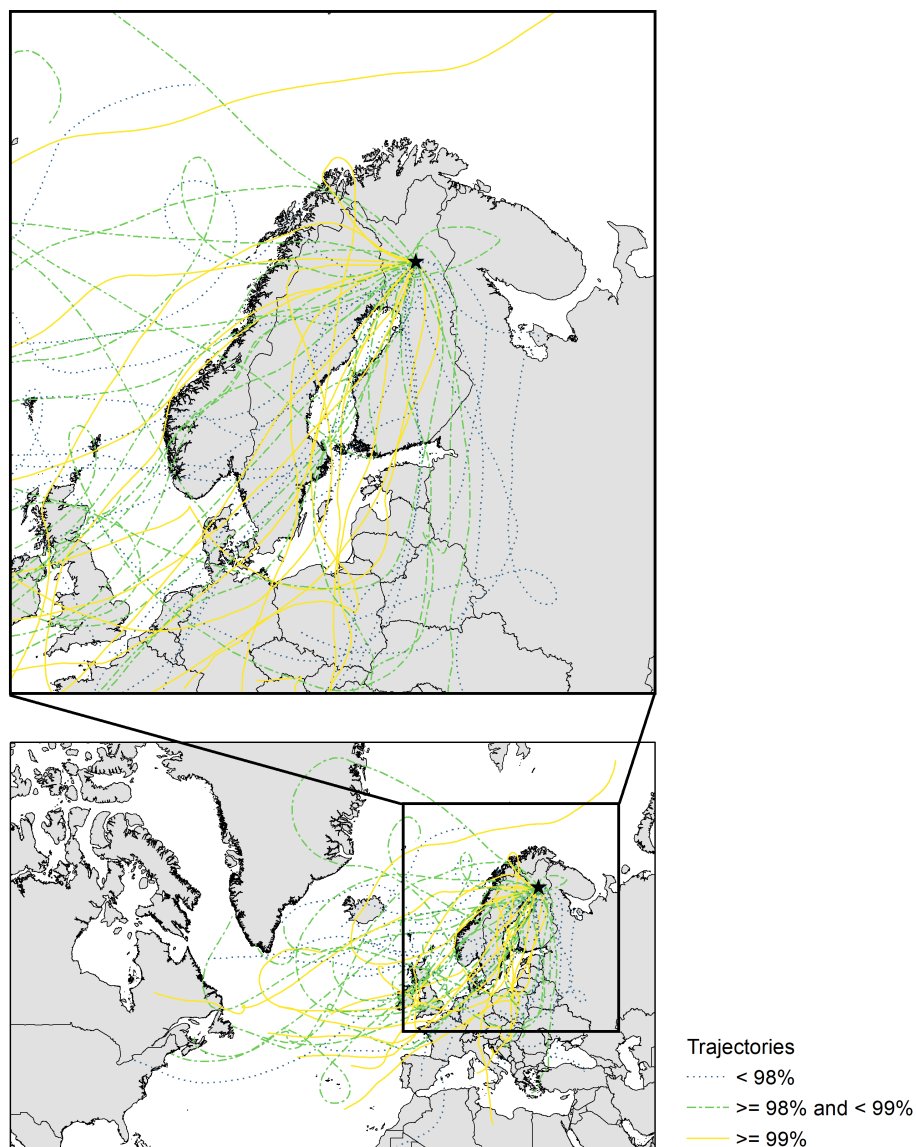
Figure 9. Five-day backward trajectories (lines) arriving at the measurement site in Sodankylä, Finland (black star) at 2.7 km above ground at full hour (i.e. 11 or 23 UTC) for each of the 52 snowfall events. The group of maximum running mean RH_{water} (as in Fig. 8) is shown in colour ($< 98\%$, dotted blue; $\geq 98\%$ and $< 99\%$, dashed green; $< 99\%$ continuous yellow). An inset map is shown in the upper panel. The trajectories were calculated using the NOAA's Hybrid Single-Particle Lagrangian Integrated Trajectory (HYSPLIT) model. One trajectory per event was computed using the GDAS one-degree meteorology dataset and the "model vertical velocity" vertical motion method.
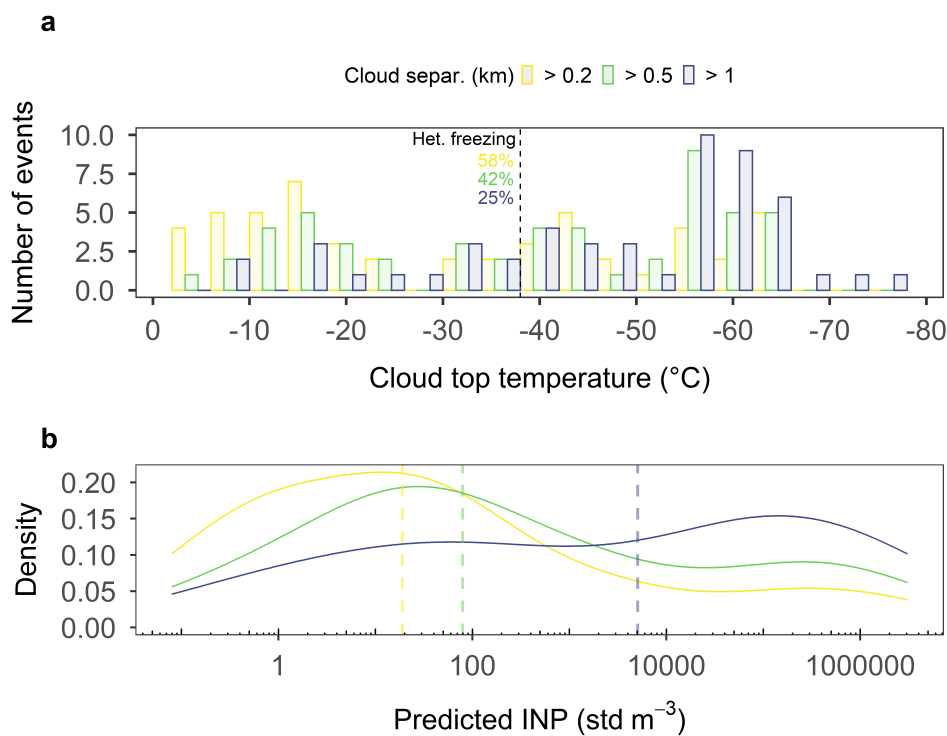
Figure 10. (a) Likely cloud top temperatures in $4\,^\circ$C intervals of the 52 events coinciding with running mean $\mathrm{RH_{ice}} \geq 97\%$ throughout the lower 2.7 km. The cloud top height was derived from the running mean $\mathrm{RH_{ice}}$. The altitude at which the running mean $\mathrm{RH_{ice}}$ fell below 100% for > 0.2 km (yellow), > 0.5 km (green), and > 1 km (blue) with increasing height was defined as cloud top height. The fraction of events with cloud top temperatures above $-38\,^\circ$C is given in percent next to the dashed line. This is an estimation of the fraction of events for which the first ice crystals were likely formed via heterogeneous freezing. **(b)** Density of the INP concentration for the fraction of events with cloud top temperatures above $-38\,^\circ$C, using the different cloud top height criteria (in color) as shown in panel a. The respective median concentrations are shown by the dashed lines.
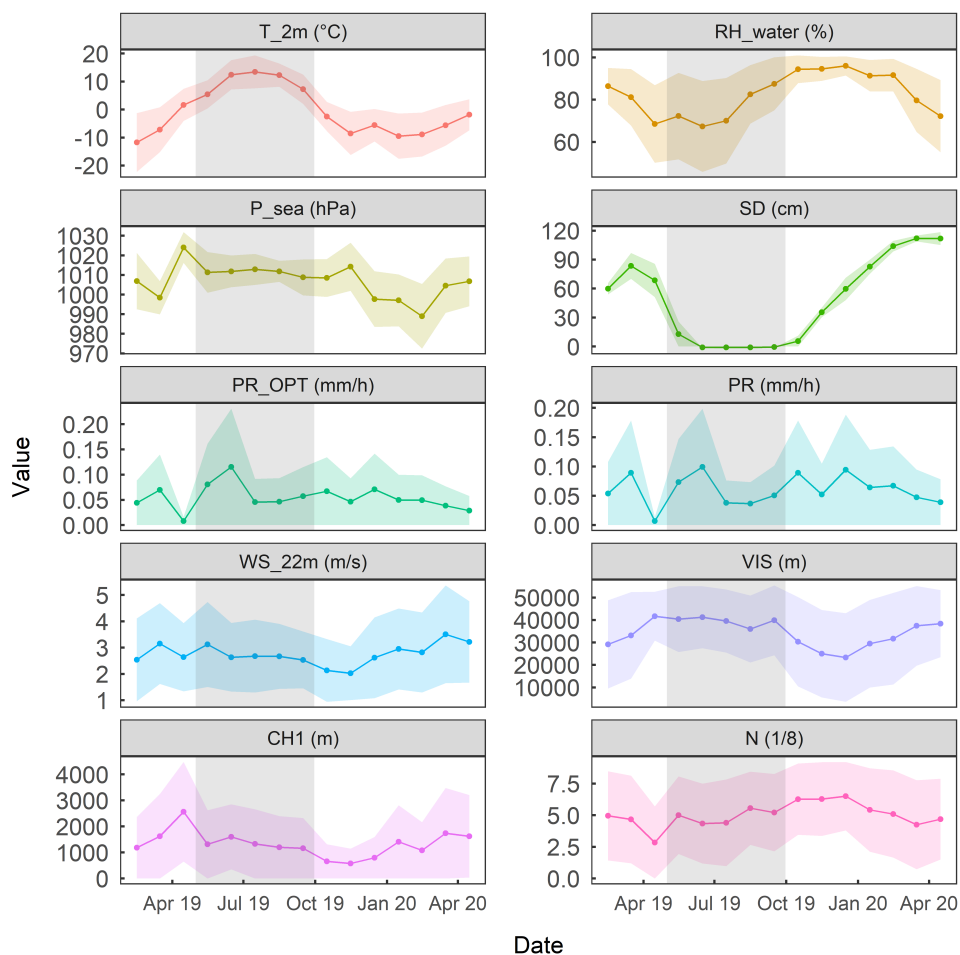
Figure A1. Time series of monthly weather parameters (means (dots and connecting lines) and standard deviations (ribbons)) at the measurement site in Sodankylä from February 2019 to April 2020. The following variables are shown (from the upper left to the bottom right): ambient air temperature at 2 m above ground (T_2m in °C), relative humidity with respect to water (RH_water in %), the pressure at sea level (P_sea in hPa), snow depth (SD in cm), precipitation rate measured optically (PR_OPT in mm h^{-1}) and by weight (PR mm h^{-1}), wind speed (WS at 22 m above ground in m s^{-1}), visibility (VIS in m), height of the lowest cloud base (CH1 in m), and total cloudiness (N, a value between 1 and 8). The grey areas lowlight the months from May to September, that were excluded from our analysis.
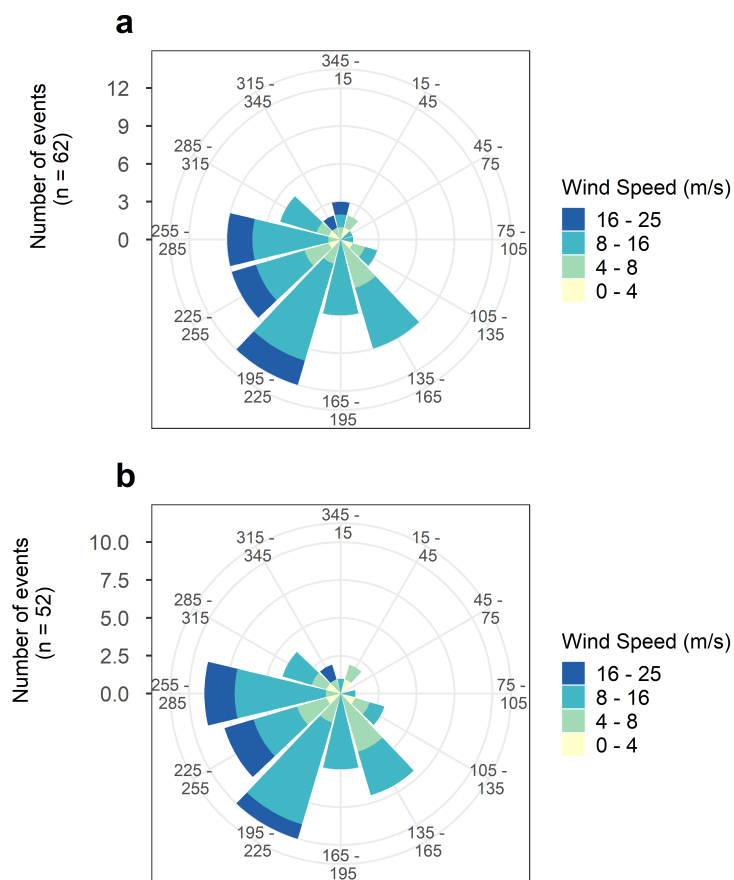
Figure A2. Wind direction measured by the radiosondes at 2.7 km of (**a**) the 62 snowfall events and (**b**) the 52 snowfall events coinciding with running mean RH$_{ice}$ ≥ 97% throughout the lower 2.7 km (see Sect. 3.2 for criterion).
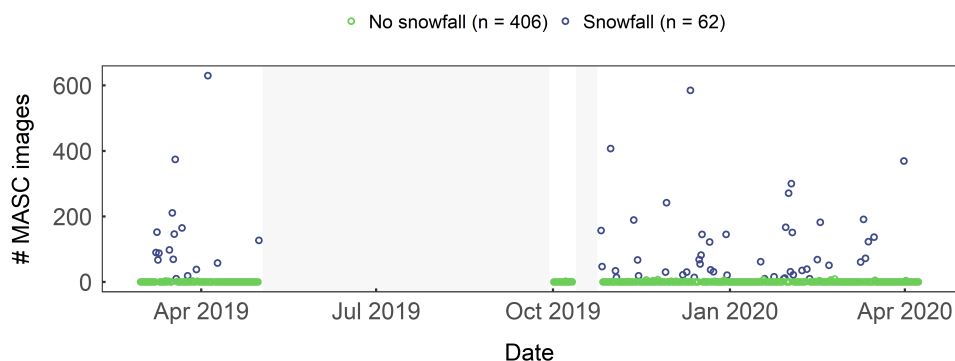
Figure A3. The number of images with objects larger than 0.54 mm^2 captured by the operational MASC instrument during coinciding radiosonde profiles from 28 February 2019 to 7 April 2020. Radiosondes were launched twice a day, at 11:30 and 23:30 UTC. Images considered were captured within a time span of 15 minutes before each radiosonde launch. Cases (i.e. 15-min time intervals) with 10 or more of such images are classified as snowfall events (n = 62, blue dots). The others are classified as no-snowfall events (n = 406, green dots). No data (gray area) was collected in the summer months (May to September) and during a technical interruption between 11 and 25 October 2019.
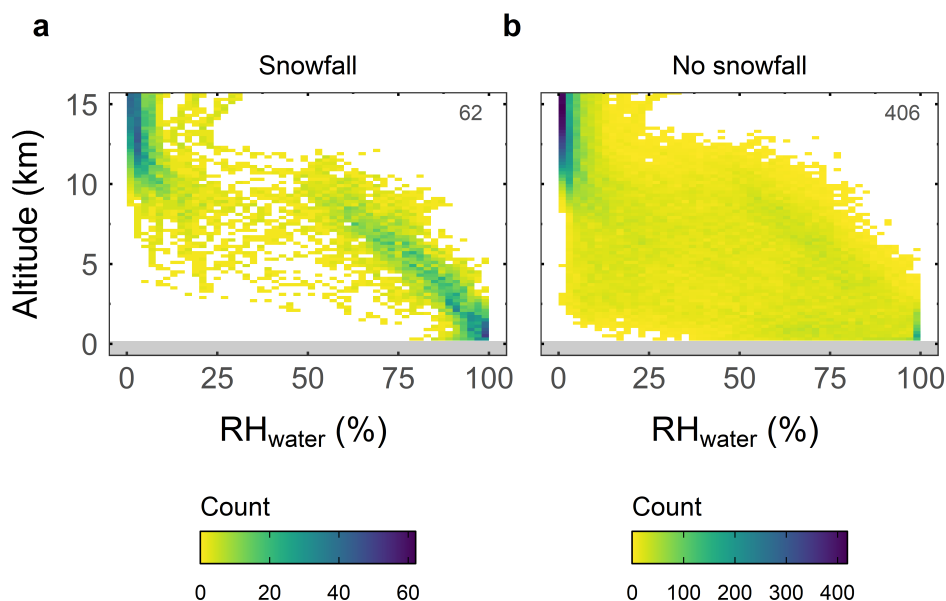
Figure A4. Same plot as Fig. 4, but for RH$_{water}$.
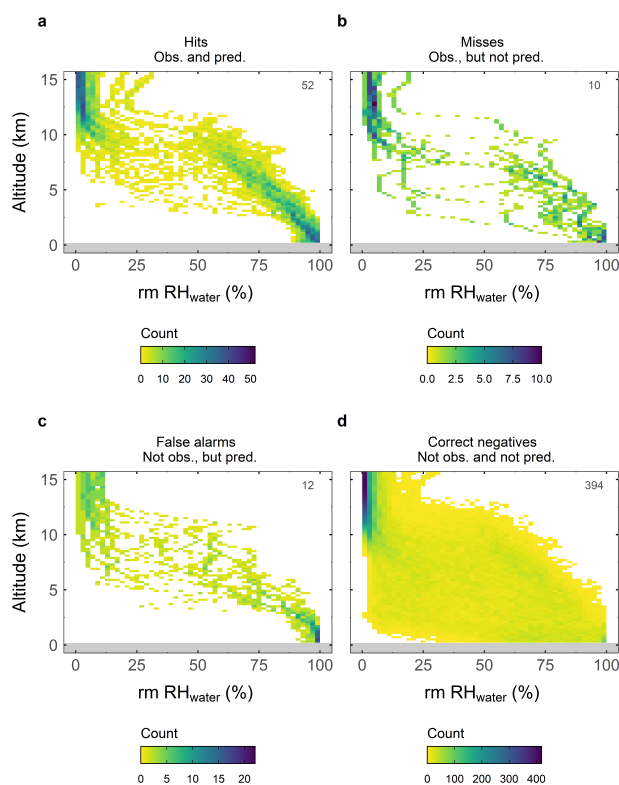
Figure A5. Same plot as Fig. 6, but for RH_{water}.
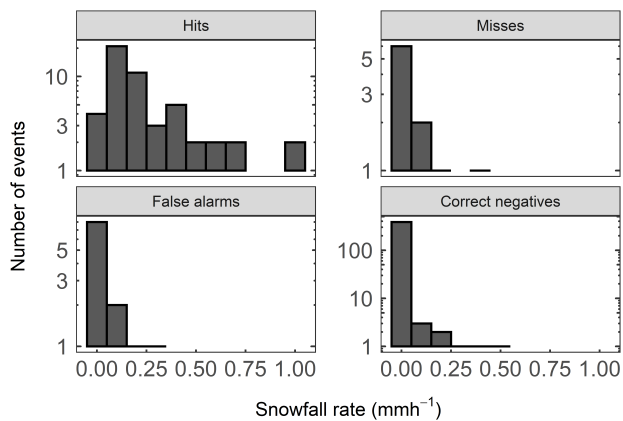
Figure A6. Snowfall rate by intervals measured optically during the events grouped by *hits*, *misses*, *false alarms*, and *correct negatives* based on the criterion running mean $RH_{ice} \geq 97\%$ throughout the lower 2.7 km to predict snowfall.
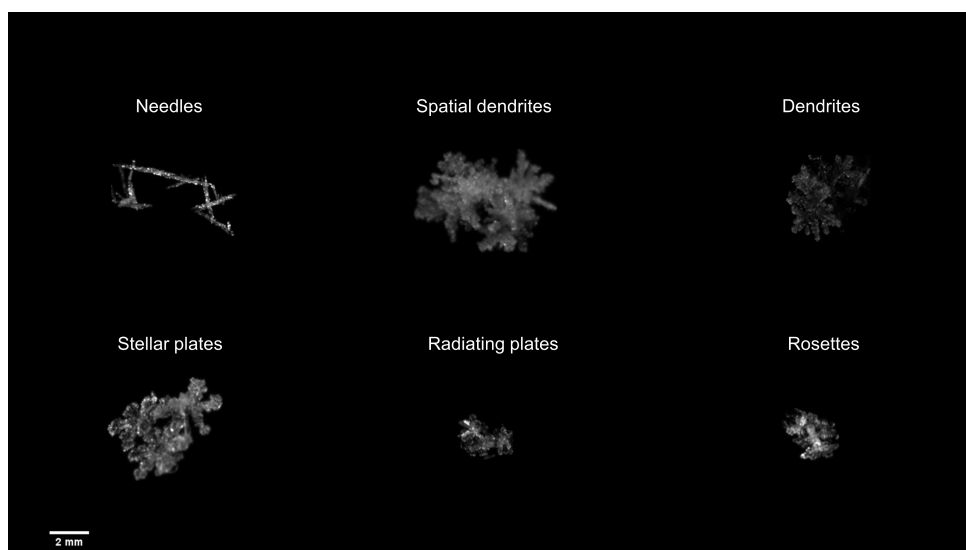
Figure A7. Similar as Fig. 7a, but for aggregates.

Table A1. Details of scores that compare observed versus predicted events. The scores are calculated with the help of hits (H), misses (M), false alarms (F), correct negatives (C), and the total number of events (Total).

Abbreviation	Name	Formula		Range	Ideal value	Reference
ACC	Accuracy	$\dfrac{H + C}{Total}$	(A1)	(0, 1)	1	Bennett et al. (2013)
CSI	Critical success index	$\dfrac{H}{H + M + F}$	(A2)	(0, 1)	1	Bennett et al. (2013)
HSS	Heidke skill score	$2\dfrac{H \cdot C - F \cdot M}{(H + M)(M + C) + (H + F)(F + C)}$	(A3)	(0, 1)	1	Hyvärinen (2014)